Braz J Phys (2014) 44:64–72
DOI 10.1007/s13538-013-0161-y

NUCLEAR PHYSICS

Decay Mechanism of $^{290,292}114^*$ Superheavy Nuclei Formed in ^{48}Ca-Induced Reactions

Kirandeep Sandhu · Manoj K. Sharma

Received: 11 March 2013 / Published online: 3 October 2013

Abstract We calculate the neutron-evaporation residue cross sections σ_{3n} , σ_{4n}, and σ_{5n} in the hot-fusion reactions ^{48}Ca+^{242,244}Pu→$^{290,292}114^*$ over a wide range of compound-nucleus excitation energies ($E^*_{\mathrm{CN}} = 34$–53 MeV). We work with the dynamical cluster-decay model (DCM), with a single parameter, the neck-length parameter ΔR. To calculate neutron-evaporation cross sections, we choose the superheavy proton magic $Z = 126$ and neutron magic $N = 184$. Among the $3n$, $4n$, and $5n$ production cross sections for $^{290,292}114^*$, only the $3n$ decay cross sections of $^{292}114^*$ correspond to spherical fragmentation. The $4n$ and $5n$ cross sections of $^{292}114^*$ and $3n$, $4n$, and $5n$ cross sections of $^{290}114^*$ could only be fitted after the inclusion of quadrupole deformations β_{2i} within the optimum orientation approach. Changes in the angular momentum and N/Z ratio do not significantly influence the fragmentation paths of $^{290,292}114^*$ superheavy nuclei. Larger barrier modification is required for the lower angular momentum states and lighter neutron clusters. The contribution of the fusion–fission component is also computed for the compound nucleus $^{292}114^*$ in the energy range $E^*_{\mathrm{CN}} =$ 27–47 MeV.

Keywords Superheavy nucleus · Neutron-evaporation residues · Fission

K. Sandhu (✉) · M. K. Sharma
School of Physics and Materials Science, Thapar University, Patiala, 147 004, Punjab, India
e-mail: kiransndh250@gmail.com

M. K. Sharma
e-mail: msharma@thapar.edu

1 Introduction

The experimental and theoretical developments in the area of heavy-ion reactions targeting the properties of nuclei located in the superheavy mass region have mainly been associated with the formation of a compound nucleus and its subsequent decay in the form of the evaporation residue and fission. During the last decade, remarkable success has been achieved regarding the formation and decay paths of superheavy nuclei using cold- and hot-fusion reactions. In order to probe the possible effect of spherical shells in the superheavy region, nuclei with $Z \geq 112$ and $N \geq 172$ must be synthesized [1]. This is hard to achieve in reactions with Pb and Bi targets. Hence, asymmetric reactions in which both the target and projectile have maximum neutron excess are preferred, such as actinide targets (Pu, Cm, and Cf) with ^{48}Ca projectile. This combination of projectiles and targets is capable of producing neutron-rich isotopes in the vicinity of $N = 184$, where relatively stable nuclear systems are expected. Several experiments have been conducted with various mass numbers for the projectile or target nuclei, which demonstrated significant stability around $N = 184$. Following this, ^{48}Ca+^{242,244}Pu→$^{290,292}114^*$ reactions were carried out to probe the stability of $Z = 114$ isotopes.

According to Hofmann [2], the calculated cross sections for ^{208}Pb(^{76}Ge, n)^{283}114 reactions are nearly negligible ($\sigma_n \geq 0.1$ pb). Therefore, cold-fusion synthesis has not been preferred to produce isotopes of $Z = 114$. Instead, hot-fusion reactions with Pu (an actinide) target were used to produce $^{290,292}114^*$ compound nuclei. Significant fusion cross sections were then observed, which provided useful information regarding the decay path and structural properties of compound nuclei corresponding to $Z = 114$.

The production of the $Z = 114$ element by ^{242}Pu bombardment with ^{48}Ca was first examined by Oganessian et al. [3]. The resulting compound nucleus, $^{290}114^*$, was investigated at different excitation energies, up to $E^*_{\rm CN} = 45$ MeV at which only $3n$ and $4n$ evaporation products were reported. Recently, Ellison et al. [4] observed a new isotope, ^{285}114, via $5n$ evaporation of $^{290}114^*$ at a relatively higher energy, of the order of 50 MeV. They reported that the $5n$ cross section, 0.6 pb for $^{290}114^*$ at 50.4 MeV, is smaller than the $3n$ and $4n$ cross sections at relatively lower energies.

Besides $^{290}114^*$, another $Z = 114$ isotope, $^{292}114^*$, has been experimentally investigated in the last decade. First, the ^{244}Pu (^{48}Ca, xn) reaction was investigated at excitation energies ranging from $E^*_{\rm CN} = 30.5$ to 53 MeV, at which Oganessian et al. [5] irradiated ^{244}Pu with ^{48}Ca to obtain $5n$ evaporation products along with $3n$ and $4n$. Recently, the ^{244}Pu (^{48}Ca, xn) reaction was further studied at excitation energies $E^*_{\rm CN} = 36.1$–39.5 MeV and $E^*_{\rm CN} = 39.8$–43.9 MeV in GSI using the TASCA recoil separator [6]. The measured neutron cross sections in Ref. [6] are higher in magnitude than the earlier reports in Ref. [5].

The above two reactions offer useful information, allowing one to investigate the relative probability of neutron evaporation along with the possible contribution of fission fragments. Fission and quasi-fission cross sections have also been reported in [7], in the energy range 27–37 MeV for $^{292}114^*$ nucleus. For an overall description of this nucleus, comprehensive knowledge of the neutron-evaporation process, along with the fission and quasi-fission (non-compound nucleus decay) processes is desirable.

Here, we rely on the dynamical cluster-decay model (DCM) [8–19] to comparatively examine the decay paths of the $^{290}114^*$ and $^{292}114^*$ superheavy nuclei formed in the ^{48}Ca-induced reactions. Our calculations are carried out in the framework of the DCM using quadrupole deformations within the optimum orientation approach, compared with the experimental data of [4, 6]. To fit the neutron-evaporation cross sections, we have chosen $Z = 126$ and $N = 184$ as proton and neutron magic numbers, since recent DCM calculations [14] have shown that $Z = 120$ (for fusion–fission data), $Z = 126$ (for fusion–evaporation data), and $N = 184$ are the optimal choices for proton–neutron magic pairs in the superheavy region. We also work out the fission cross sections for the $^{292}114^*$ compound nucleus in the 27- to 47-MeV energy range by letting $Z = 120$ and $N = 184$ be the superheavy magics. An earlier test of the DCM considering the ^{48}Ca+^{244}Pu reaction in reference to the data of [5] and [7] has been presented in Ref. [16].

In a recent work [17] focusing on the $^{297}117^*$ formed in the ^{48}Ca+^{249}Bk reaction, we used the DCM to account for $2n$, $3n$, and $4n$ decay cross sections and showed that ^{4}He contributed towards the $4n$ decay channel. No analogous ^{4}He contribution is seen in either of the $^{290}114^*$ and $^{292}114^*$ compound nuclei over a wide range of incident energies.

The paper is organized as follows: Section 2 gives a brief account of the DCM, extended to include the deformations and orientation effects of the outgoing channel. The calculations and discussion are presented in Section 3. Finally, the results are summarized in Section 4.

2 The DCM

The DCM [8–19], which finds its basis in the preformed cluster model (PCM) [20–22], is expressed in terms of the collective coordinates of mass and charge asymmetries $\eta = (A_1 - A_2)/(A_1 + A_2)$ and $\eta_Z = (Z_1 - Z_2)/(Z_1 + Z_2)$, respectively, the relative separation R, the multipole deformations $\beta_{\lambda i}(\lambda = 2, 3, 4, ...)$, and the orientations θ_i ($i = 1, 2$) of two nuclei or fragments, where 1 and 2 denote the heavy and light fragments, respectively. The PCM is applicable to ground-state decays, such as α and cluster decays, spontaneous fission, etc., whereas DCM is applicable to the dynamics of the hot and rotating compound systems formed in heavy-ion reactions. Under partial-wave decomposition, the compound-nucleus decay cross section is given the expression

$$\sigma = \sum_{\ell=0}^{\ell_{\max}} \sigma_\ell = \frac{\pi}{k^2}\sum_{\ell=0}^{\ell_{\max}}(2\ell+1)P_0 P; \quad k = \sqrt{\frac{2\mu E_{\rm c.m.}}{\hbar^2}}. \quad (1)$$

The preformation probability P_0 refers to the η motion and the penetrability P to the R motion, both dependent on the angular momentum ℓ and temperature T.

In Eq. (1), $\mu \equiv \frac{A_1 A_2}{A_1+A_2}m$ is the reduced mass, with m as the nucleon mass. The maximum angular momentum $\ell_{\max}$ is fixed by the vanishing of the light-particle—here, neutron—cross section, i.e., $\sigma_{ER} \equiv \sigma_{xn}$ (x = 3, 4, or 5) becoming negligibly small at $\ell = \ell_{\max}$. The preformation probability P_0, which represents the probability of forming the decaying fragment at the compound-nucleus state, is given by the equality

$$P_0 = \mid \psi_R(\eta(A_i)) \mid^2 \sqrt{B_{\eta\eta}}\frac{2}{A_{\rm CN}}. \quad (2)$$

The probability P_0 contains important information regarding the structural features of the decaying nucleus. To compute it, we solve the stationary Schrödinger equation in η, at fixed $R = R_{\rm a}$:

$$\left\{-\frac{\hbar^2}{2\sqrt{B_{\eta\eta}}}\frac{\partial}{\partial\eta}\frac{1}{\sqrt{B_{\eta\eta}}}\frac{\partial}{\partial\eta} + V(R,\eta,T)\right\}\psi^\nu(\eta) = E^\nu\psi^\nu(\eta), \quad (3)$$

where

$$R_a = R_1(\alpha_1, T) + R_2(\alpha_2, T) + \Delta R(T) \tag{4}$$

The mass parameters $B_{\eta\eta}$ are the smooth hydrodynamical masses [23]. The fragmentation potential $V(R, \eta, T)$ on the left-hand side of Eq. (3) is defined as follows:

$$\begin{aligned} V(R, \eta, T) = & \sum_{i=1}^{2} [V_{\mathrm{LDM}}(A_i, Z_i, T)] \\ & + \sum_{i=1}^{2} [\delta U_i] \exp\left(-T^2/T_0^2\right) \\ & + V_C(R, Z_i, \beta_{\lambda i}, \theta_i, T) \\ & + V_P(R, A_i, \beta_{\lambda i}, \theta_i, T) \\ & + V_\ell(R, A_i, \beta_{\lambda i}, \theta_i, T), \end{aligned} \tag{5}$$

where V_{LDM} and δU are the T-dependent liquid-drop and shell correction energies, respectively, taken from Refs. [24] and [25]. V_C, V_P, and V_ℓ are the T- and ℓ-dependent Coulomb, nuclear proximity, and angular momentum-dependent potentials for deformed and oriented nuclei, respectively.

The penetrability P in Eq. (1) is calculated with the WKB integral

$$P = \exp\left[-\frac{2}{\hbar} \int_{R_a}^{R_b} (2\mu[V(R) - Q_{\mathrm{eff}}])^{1/2} dR\right], \tag{6}$$

where R_b is the second turning point, which satisfies the equality

$$V(R_a, \ell) = V(R_b, \ell) = Q_{\mathrm{eff}}(T, \ell) = \mathrm{TKE}(T). \tag{7}$$

The radius R_a, defined by Eq. (4), is the first turning point of the penetration path, as illustrated in Fig. 1 for the $3n$ decay of $^{290}114^*$ and $^{292}114^*$ at two extreme ℓ values. The

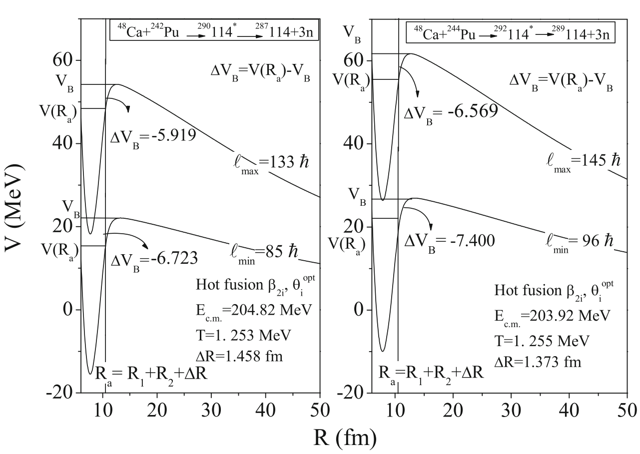

Fig. 1 Scattering potential for the decay ^{48}Ca+^{242,244}Pu $\rightarrow^{290,292}$ $114^* \rightarrow^{287,289}$114+3$n$ at two extreme ℓ values, the ℓ_{max} and the ℓ_{min}

radius vector $R_i(\alpha_i, T)$ for the deformed nucleus is defined by the expression

$$R_i(\alpha_i, T) = R_{0i}(T)\left[1 + \sum_{\lambda} \beta_{\lambda i} Y_\lambda^{(0)}(\alpha_i)\right], \tag{8}$$

where

$$R_{0i}(T) = \left[1.28 A_i^{1/3} - 0.76 + 0.8 A_i^{-1/3}\right](1 + 0.0007T^2). \tag{9}$$

Here, T (in megaelectron volts) is given by the center-of-mass energy $E_{\mathrm{c.m.}}$ and the incoming channel Q_{in}, since $E^*_{\mathrm{CN}} = E_{\mathrm{c.m.}} + Q_{\mathrm{in}} = (A_{\mathrm{CN}}/a)T^2 - T$, with the level-density parameter $a = 9 - 11$, depending on the mass A_{CN} of the compound nucleus. In our calculations, $a = 11$. For the deformation $\beta_{\lambda i}$, we use β_{2i} only, taken from [26], and the orientations θ_i are the "optimal" orientations θ_i^{opt} of the "hot fusion" process, taken from [27]. The neck-length parameter ΔR, defined in Eq. (4), is the relative separation distance between two fragments or clusters A_i and has been shown to assimilate neck-formation effects [28–30]. The parameter ΔR determines the first barrier-penetration turning point and is associated with actual barrier height and consequently with the concept of "barrier lowering" [better defined, below, by Eq. (10)]. The neck-length parameter, or equivalently "barrier modification," helps us to account for the fusion hindrance phenomenon at sub-barrier energies. The inclusion of ΔR significantly modifies the effective potential. The fitted ΔR allows us to define the effective barrier-lowering parameter $\Delta V_B(\ell)$ for each ℓ as the difference between the actual barrier $V(R_a, \ell)$ and the top of the calculated barrier $V_B(\ell)$:

$$\Delta V_B(\ell) = V(R_a, \ell) - V_B(\ell). \tag{10}$$

Since ΔV_B is negative, the actual barrier is lower than $V_B(\ell)$, as shown in Fig. 1 for both $Z = 114$ isotopes at extreme ℓ values.

3 Results and Discussions

The decay of the compound nuclei $^{290,292}114^*$ in the hot-fusion reactions ^{48}Ca+^{242,244}Pu has been studied experimentally in [4, 6]. The fusion–evaporation residue cross sections ($\sigma_{xn} = 3n$, $4n$, and $5n$) were measured at different excitation energies in the E^*_{CN} range of 34–53 MeV. From this data, we attempt to understand the decay paths of the $Z = 114$ isotopes with $A = 290$ and 292 using the DCM, the deformation, and the orientation effects of decaying fragments being appropriately incorporated. We let $Z = 126$ and $N = 184$ be the proton and neutron magic shell closures, in view of recent calculations in the superheavy mass region based on the DCM [14]. Reference [14] suggested $Z = 120$ and $N = 184$ for fusion–fission data and $Z = 126$ or 120 and $N = 184$ for fusion–evaporation data as the best possible choices for the proton and neutron magic pairs in the superheavy mass region. For this reason, to fit the fusion fission data of $^{292}114^*$, we have chosen $Z = 120$ and $N = 184$ as the superheavy magic shell closure.

We first examine the fragmentation potential $[V(A_2)]$ plots in Fig. 2a–c for $^{290}114^*$ and Fig. 2d–f for $^{292}114^*$, at the two extreme angular momenta, $\ell = 0$ and $\ell_{\max}$, for $3n$, $4n$, and $5n$ decays, at comparable energies. The following aspects of Fig. 2 merit special attention: (1) The fragmentation paths for $^{290}114^*$ and $^{292}114^*$ yield similar behaviors for $3n$, $4n$, and $5n$ decays, independently of the projectile energy; (2) strong minima result for the evaporation residues as well as for the fission fragments with $A_2 > 130$, within the heavy-mass fragment (HMF) window $80 \leq A_2 \leq 90$; (3) for all evaporation channels, the structure of V(A_2) is nearly independent of ℓ; and (4) a reaction valley (potential minimum) is consistently seen for the $^{48}Ca+^{242,244}Pu$ channels, for $^{290}114^*$ and $^{292}114^*$, respectively.

Additional understanding of these results comes from the preformation factor $P_0(A_i)$ in Fig. 3, which compares the preformation probabilities at $\ell = 0$ and $\ell_{\max}$ for the $3n$, $4n$, and $5n$ decay channels, for $^{290}114^*$ in Fig. 3a–c and for $^{292}114^*$ in Fig. 3d–f. The preformation probability is calculated from the temperature-dependent potentials of Eq. (5) in the Schrödinger equation (Eq. (3)). Consequently, an appropriate preformation probability is obtained at the assigned temperature/energy. Clearly, the mass distribution is asymmetric for both isotopes of $Z = 114$. The maximum preformation probability is obtained for the evaporation residues, HMF window $A_2 = 80$–90 and for fission fragments (near the fragment mass $A_2 \pm 26$). Independently of the decay channel, the local maxima at $^{48}Ca+^{242,244}Pu$ decay channels are seen for $^{290}114^*$ and $^{292}114^*$, respectively, in agreement with our discussion of Fig. 2.

The ℓ states contributing to the cross sections are in the window $\ell_{\min} \leq \ell \leq \ell_{\max}$. The contributions of angular momenta below $\ell_{\min}$ or above $\ell_{\max}$ are negligible. To determine the ℓ window, we plot the cross sections for various evaporation residue channels and fix the limiting values for each decay. The result is depicted in Fig. 4, where the $3n$, $4n$, and $5n$ cross sections are plotted as functions of ℓ for the $^{290,292}114^*$ compound nuclei, with the cutoff point fixed at $\sigma_{xn} < 10^{-15}$ mb and the ℓ window determined by the above-described procedure. Comparison between the

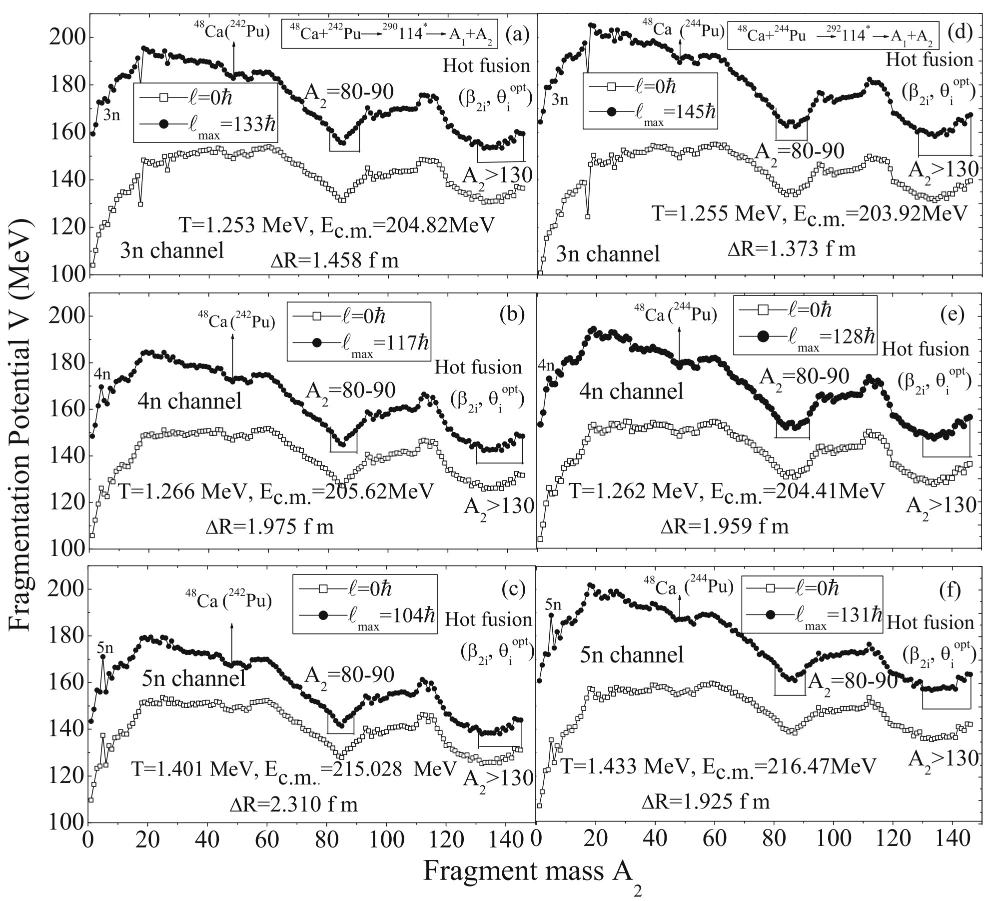

Fig. 2 Fragmentation potentials for $^{48}Ca+^{242,244}Pu \rightarrow ^{290,292}114^*$ reactions as functions of the light-mass fragment A_2 for various neutron-evaporation channels with β_{2i} deformations and "optimum" orientations θ_i^{opt} at $\ell = 0$ and $\ell_{\max}$ values

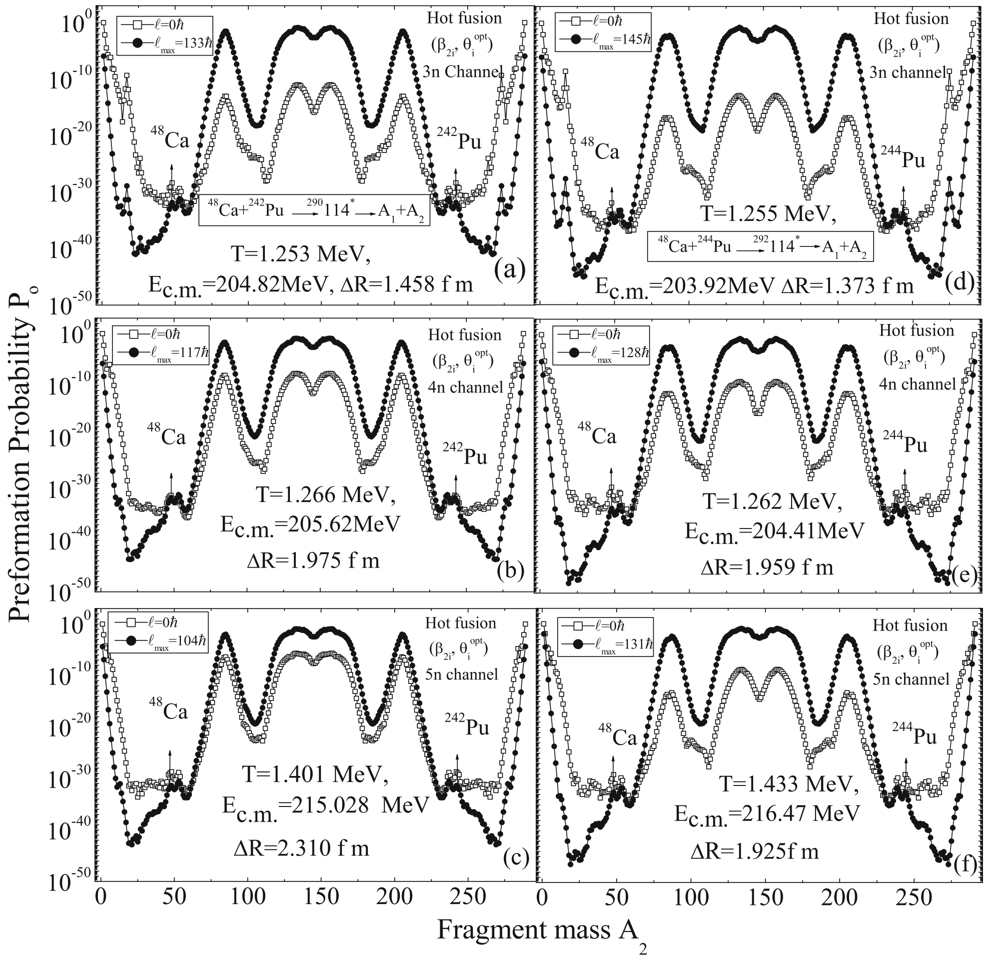

Fig. 3 Preformation probabilities for ^{48}Ca+^{242,244}Pu→^{290,292}114* reactions as a function of the light-mass fragment A_2 for various neutron-evaporation channels at $\ell = 0$ and $\ell_{\max}$, with the neck-length parameter ΔR fitted to the deformed case

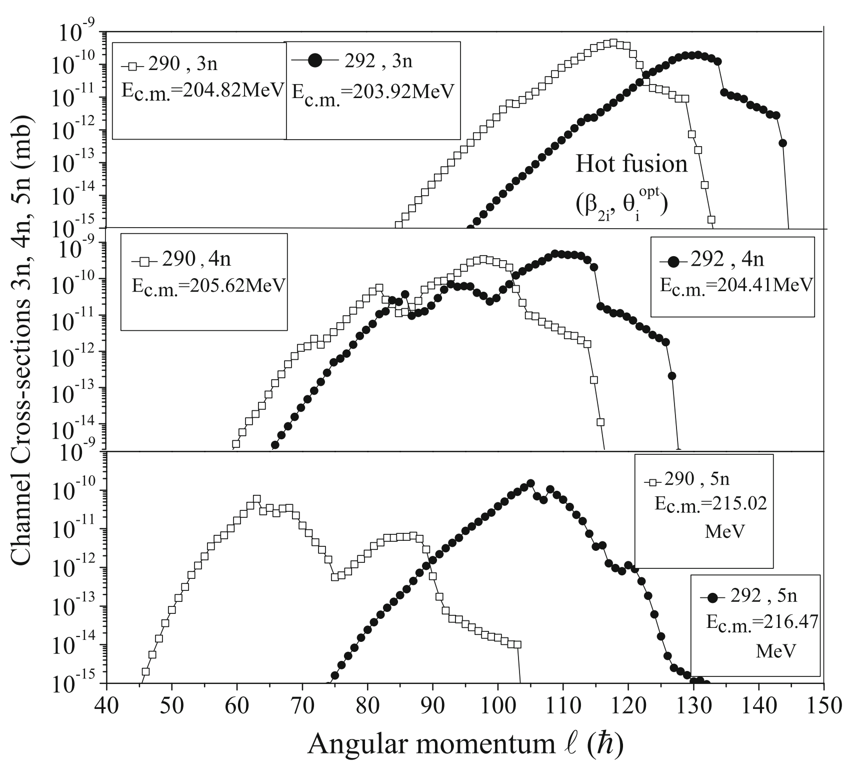

Fig. 4 Channel cross section σ_{xn} as a function of ℓ. The cutoff point, which limits the minimum and maximum angular momenta $\ell_{\min}$ and $\ell_{\max}$, is $\sigma_{xn} < 10^{-15}$ mb

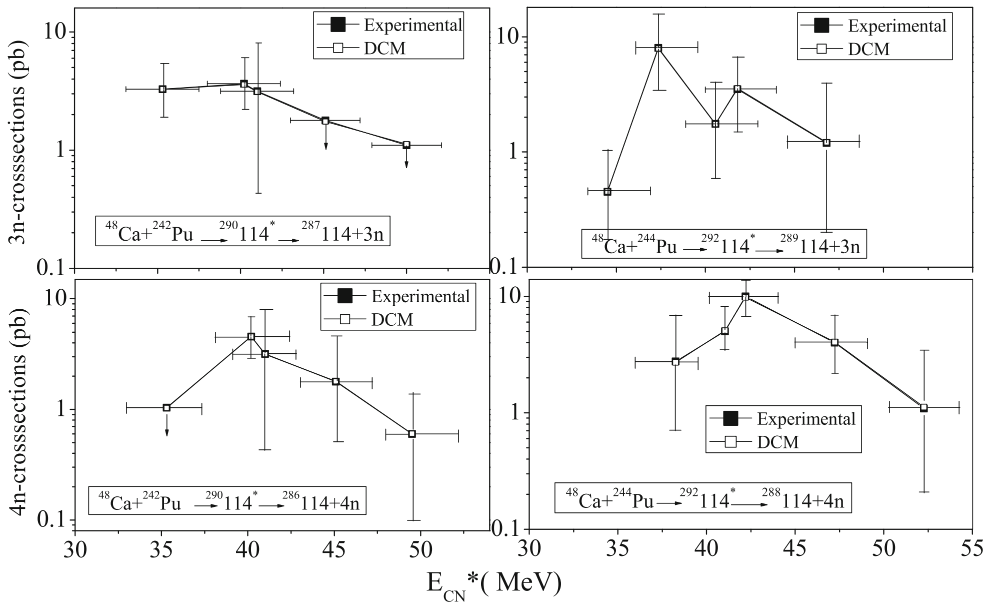

Fig. 5 DCM-calculated cross sections σ_{3n} and σ_{4n} for the decay of $^{290,292}114^*$, plotted as a function of $E^*_{\rm CN}$ and compared with the experimental data

$^{292}114^*$ compound nucleus and the $^{290}114^*$ superheavy compound nucleus shows that, for the same energy range, the angular momenta contributing to the former are higher than the ℓ values contributing to the latter. The ℓ window for the $3n$, $4n$, and $5n$ decay channels are in the ranges (85–145), (59–128), and (45–132), respectively. As discussed in Ref. [17], $\ell_{\rm min}$ and $\ell_{\rm max}$ can be independently estimated by plotting the penetrability P and preformation probability P_o as functions of ℓ. The penetrability plot determines $\ell_{\rm min}$, and the preformation plot determines $\ell_{\rm max}$. In the resulting range $\ell_{\rm min} \le \ell \le \ell_{\rm max}$, the preformation and penetration probabilities contribute significantly to the cross section and offer an estimate of the total decay cross sections.

The DCM cross sections are compared in Fig. 5 with the experimental data of Refs. [4, 6] for $3n$ and $4n$ decays. The $5n$ decay channel is omitted from Fig. 5 because data is available at one point only, which is shown in Tables 1 and 2 for $^{290}114^*$ and $^{292}114^*$, respectively. Figure 5 clearly shows that the DCM can reproduce the neutron-evaporation residue cross-sectional data over a wide range of center-of-mass energies with a single fitting parameter, the neck-length parameter ΔR. The relevant details of the calculations are also shown in Tables 1 and 2 for the $^{290}114^*$ and $^{292}114^*$ superheavy nuclei, respectively.

Figure 6 shows the barrier-lowering parameter ΔV_B as a function of $E^*_{\rm CN}$, for $3n$ and $4n$ evaporation at $\ell = \ell_{\rm max}$. The ΔV_B for the $^{290}114^*$ and $^{292}114^*$ superheavy nuclei is

Table 1 Experimental and DCM-calculated evaporation residue cross sections σ_{xn}, x = 3, 4, and 5 in the decay of $^{290}114^*$ formed in the ^{48}Ca+^{242}Pu reaction

$E^*_{\rm CN}$ (MeV)	xn	T (MeV)	$\ell_{\rm max}$ ($\hbar$)	ΔR (fm)	$\sigma^{\rm DCM}_{xn}$ (pb)	$\sigma^{\rm Expt.}_{xn}$ (pb)
35.3	$3n$	1.176	130	1.490	3.28	3.29
	$4n$		114	1.951	1.03	1.04
40.2	$3n$	1.253	133	1.458	3.60	3.66
	$4n$		115	2.026	4.58	4.56
41.0	$3n$	1.266	134	1.450	3.12	3.16
	$4n$		117	1.975	3.16	3.18
45.1	$3n$	1.327	135	1.417	1.75	1.79
	$4n$		122	1.883	1.79	1.78
50	$3n$	1.396	137	1.375	1.13	1.10
49.5	$4n$	1.389	128	1.733	0.604	0.6
50.4	$5n$	1.401	104	2.310	0.434	0.6

Table 2 Experimental and DCM-calculated evaporation residue cross sections σ_{xn}, x = 3, 4, and 5 in the decay of $^{292}114^*$ formed in the ^{48}Ca+^{244}Pu reaction

$E^*_{\rm CN}$ (MeV)	xn	T (MeV)	$\ell_{\rm max}$ ($\hbar$)	ΔR (fm)	$\sigma^{\rm DCM}_{xn}$ (pb)	$\sigma^{\rm Expt.}_{xn}$ (pb)
34.51	$3n$	1.158	143	1.352	0.455	0.452
37.35	$3n$	1.205	142	1.459	7.92	8.03
38.26	$4n$	1.219	128	1.921	2.72	2.75
40.56	$3n$	1.255	145	1.373	1.74	1.75
41.05	$4n$	1.262	128	1.959	5.06	5.08
41.8	$3n$	1.278	146	1.394	3.57	3.52
42.20	$4n$	1.279	126	2.036	9.83	9.91
46.8	$3n$	1.346	148	1.337	1.21	1.20
47.23	$4n$	1.352	134	1.867	4.06	4.00
52.56	$4n$	1.426	138	1.731	1.12	1.10
53.11	$5n$	1.433	131	1.925	1.11	1.11

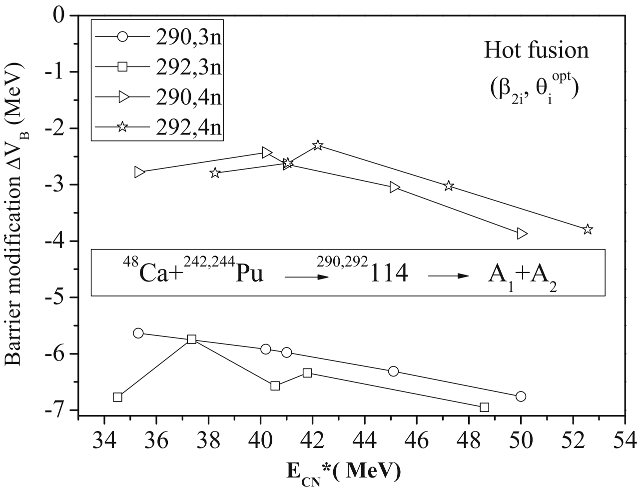

Fig. 6 Barrier modification ΔV_B as a function of $E^*_{\rm CN}$ for $3n$ and $4n$ decays of compound nuclei $^{290,292}114^*$ at $\ell = \ell_{\max}$

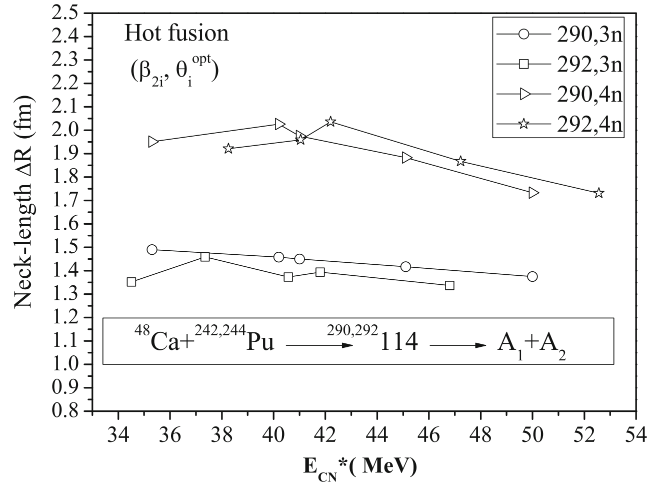

Fig. 8 ΔR as a function of $E^*_{\rm CN}$ for $3n$ and $4n$ decays of the compound nuclei $^{290,292}114^*$

comparable, for the $3n$ as well as for the $4n$ decay channel. The barrier modification for $3n$ decay is higher than that for the $4n$ decay path. Interestingly, ΔV_B shows little dependence on the compound-nucleus energy, for either of the decay channels. The barrier modification is a built-in property of the DCM, which depends on the fitting of neck-length parameter ΔR. Figure 7 shows the dependence of the barrier-lowering parameter ΔV_B on the angular momentum, for the $3n$ and $4n$ decay channels, at comparable energies. ΔV_B decreases as ℓ grows, independently of decay channel, i.e., lower angular momentum states require larger "barrier modifications."

The neck-length parameter ΔR, which fixes the barrier-lowering parameter ΔV_B, is chosen to optimize the fit to neutron-evaporation residue data, which is plotted as a function of $E^*_{\rm CN}$ in Fig. 8 for ^{48}Ca+^{242,244}Pu→$^{290,292}114^*$

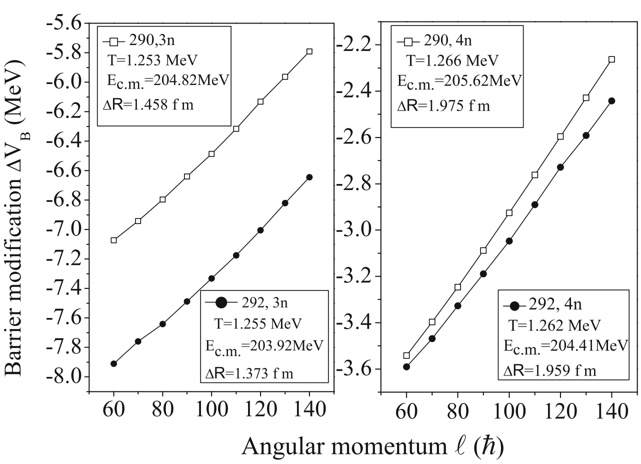

Fig. 7 ΔV_B as a function of ℓ for $3n$ and $4n$ decays of compound nuclei $^{290,292}114^*$

reactions. The plots offer systematic information on the timescale at which the neutrons are emitted from $^{290}114^*$ and $^{292}114^*$ nuclei. The neck-length parameter ΔR for $3n$ and $4n$ decay paths is comparable, for either the $^{290}114^*$ or the $^{292}114^*$ superheavy nuclei. Independently of the mass of the $Z = 114$ nucleus, the magnitude of ΔR for the $4n$ decay channel is higher than that for $3n$ decay path. For the $5n$ decay path, ΔR is highest for $^{290}114^*$. For the $^{292}114^*$ system, it is comparable to that for $4n$ decay channel. ΔR for the $5n$ channel is not shown in Fig. 8 because data is available at one energy only.

To fit the $3n$, $4n$, and $5n$ cross sections for the decay of $^{290}114^*$ and $^{292}114^*$ superheavy nuclei, we had to allow deformation-effects, except for the $3n$ decay of the $^{292}114^*$ nucleus. In other words, only the $3n$ decay of $^{292}114^*$ can be fitted with spherical fragmentation. This gives information on the effect of deformation in the decay of the $^{292}114^*$ compound nucleus.

Figure 9a shows the mass fragmentation potentials $V(A_2)$ for $^{292}114^*$ at $\ell = \ell_{\max}$ for the spherical and the deformed fragmentation approaches. The deformations are included up to β_{2i}, with optimal orientation, at the highest energy $E^*_{\rm CN} = 46.8$ MeV and $T = 1.346$ MeV for $3n$ evaporation residue product. Comparison between the results for the two fragmentation potentials shows that $\ell_{\max}$ for spherical fragmentation is smaller than the maximum angular momentum for deformed fragmentation. In the former case, the mass fragmentation is relatively smooth, without marked dips, whereas β_{2i} introduces more structure in the fragmentation path. The spherical fragmentation seems to prefer symmetric fission, whereas the β_2 deformations lead to the emergence of asymmetric components. The relevant details of spherical fragmentation for the $^{292}114^*$ system are presented in Table 3.

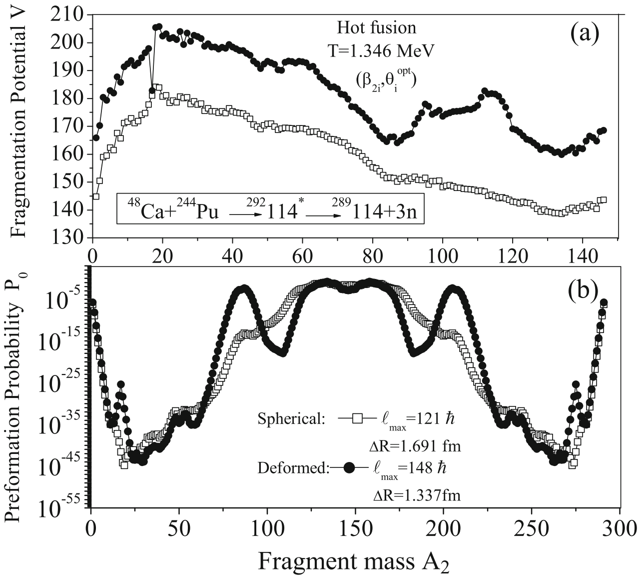

Fig. 9 Fragmentation and preformation potentials for the ^{48}Ca+^{244}Pu→^{292}114* reaction as functions of the light-mass fragment (A_2) for the $3n$ neutron-evaporation channel for spherical nuclei and for deformed nuclei with β_{2i} deformations and optimum orientations θ_i^{opt} at $\ell = \ell_{max}$

Additional enlightenment comes from the preformation probability of ^{292}114* for the $3n$ decay channel at $\ell = \ell_{max}$. It is clear from Fig. 9b that the preformation probability is nearly symmetric for the spherical case and becomes relatively asymmetric with the inclusion of deformation effects. In the framework of the DCM, the spherical fragmentation fails for the $3n$, $4n$, and $5n$ decays of compound nucleus ^{290}114* and for the $4n$ and $5n$ decays of ^{292}114*; it only commences for the $3n$ decay of ^{292}114* nucleus. We conclude that deformation effects are capitally important in the study of the decay paths of the $Z = 114$ isotopes formed in ^{48}Ca-induced reactions.

To study the N/Z ratio dependence, we have added and subtracted two successive neutrons to the different $Z = 114$ compound nuclei. Figures 2 and 3 compared ^{290}114* and ^{292}114* for $3n$, $4n$, and $5n$ decays. We now consider two other isotopes of $Z = 114$ nuclei, with $A_2 = 288$ and 294. We only carry out the isotopic analysis for $3n$ decay by extrapolating the neck-length parameter ΔR obtained for ^{290}114* and ^{292}114* at $T \approx 1.25$ MeV. Figure 10a represents the fragmentation potential as a function of the fragment mass A_2 for different isotopes of $Z = 114$ superheavy nucleus at $T \approx 1.25$ MeV. Broadly speaking, the fragmentation path is quite similar when two neutrons are subsequently added to $Z = 114$ and $N = 174$, i.e., to the ^{288}114* nucleus, to form the ^{290}114*, ^{292}114*, and ^{294}114* nuclei.

Slight variations are seen in the HMF and fission region, but the general trends are similar. We conclude that the addition of two, four, and six neutrons to the ^{288}114* compound nucleus, i.e., changing the N/Z ratio, introduces only small, not very significant changes in the fragmentation path of the HMF and fission fragments of different compound nuclei corresponding to $Z = 114$, but no such changes are observed for the evaporation residue region.

To further compare the behaviors of different $Z = 114$ isotopes, we examine the preformation probability. The preformation probabilities for ^{288}114*, ^{290}114*, ^{292}114*, and ^{294}114* compound nuclei almost overlap with each other, an indication that the preformation is identical for all the fragments. On the basis of the fragmentation behavior in Fig. 10a and preformation probability in Fig. 10b, we conclude that changes in the N/Z ratio bear no significant influence upon the decay paths of the $Z = 114$ superheavy nuclei isotopes.

Table 3 Experimental and DCM-calculated evaporation residue cross sections σ_{xn} ($x = 3$) for spherical fragmentation in the decay of ^{292}114* formed in the ^{48}Ca+^{244}Pu reaction

E^*_{CN} (MeV)	T (MeV)	ℓ_{max} ($\hbar$)	ΔR (fm)	σ^{DCM}_{xn} (pb)	$\sigma^{Expt.}_{xn}$ (pb)
34.51	1.158	112	1.769	0.460	0.452
37.35	1.205	106	2.005	7.98	8.03
40.56	1.255	115	1.780	1.72	1.75
41.8	1.278	116	1.812	3.52	3.52
46.8	1.346	121	1.691	1.14	1.20

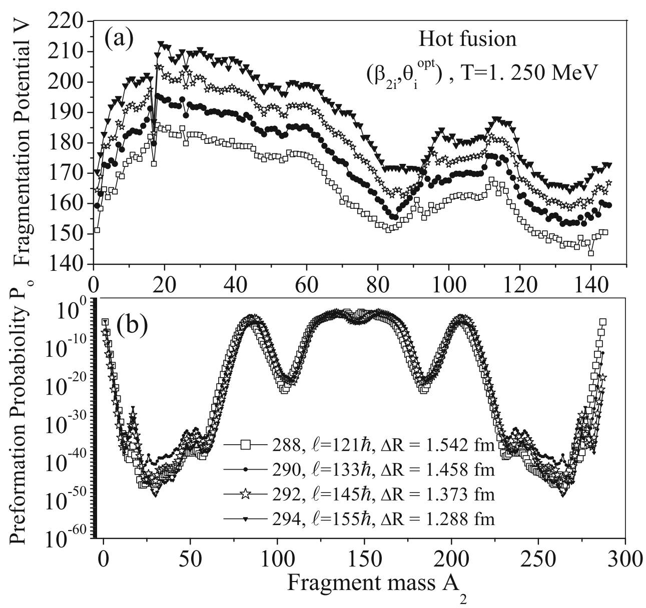

Fig. 10 Fragmentation and preformation potentials for $Z = 114$ isotopes as functions of the light-mass fragment A_2 for the $3n$ neutron-evaporation channel, using β_{2i} deformations and optimal orientations θ_i^{opt} for hot fusion at $\ell = \ell_{max}$

Table 4 Experimental and DCM-calculated fission and quasi-fission cross sections in the decay of $^{292}114^{*}$ formed in the ^{48}Ca+^{244}Pu reaction

E^{*}_{CN} (MeV)	$\ell_{\max}$ ($\hbar$)	ΔR_{f} (fm)	$\sigma_{\mathrm{f}}^{\mathrm{DCM}}$ (mb)	$\sigma_{\mathrm{f}}^{\mathrm{Expt.}}$ (mb)	ΔR_{qf} (fm)	$\sigma_{\mathrm{qf}}^{\mathrm{DCM}}$ (mb)	$\sigma_{\mathrm{qf}}^{\mathrm{Expt.}}$ (mb)
27.4	143	0.924	0.166	0.175	0.710	1.4	1.39
30.3	147	0.931	0.486	0.491	0.790	4.86	4.86
37.0	152	0.941	4.1	4.1	0.908	26.6	26.6
40.5	154	0.946	7.56	–	0.970	54.8	–
41.8	155	0.948	10.9	–	0.990	70.3	–
46.8	156	0.955	16.2	–	1.080	186	–

After applying the DCM to 3n, 4n, and 5n decay paths of $^{290}114^{*}$ and $^{292}114^{*}$ nuclei, we have also calculated the fission (σ_{f}) and quasi-fission (σ_{qf}) cross sections for $^{292}114^{*}$, to compare with the experimental data in Ref. [7], which report these cross sections at three different energies, i.e., 27.4, 30.3, and 37 MeV. First, to fix the neck-length parameter ΔR for the aforementioned fission data, listed in Table 4, we have chosen $Z = 120$ and $N = 184$ as possible magic numbers, for the reason mentioned in Section 1. After estimating σ_{f} and σ_{qf} in the 27–37-MeV energy range, we have extrapolated the neck-length parameter ΔR to the energy range 40–47 MeV.

The resulting fission and quasi-fission cross sections are shown in Table 4. The fragments in the mass range $(A/2) \pm 26$ contribute to the fission cross section. The quasi-fission cross sections are estimated by setting $P_0 = 1$ for the outgoing fragment ^{48}Ca+^{244}Pu, assuming that the fragments do not lose their identity in the quasi-fission process.

4 Summary

We have used the DCM to calculate the 3n, 4n, and 5n decay cross sections for $^{48}\mathrm{Ca}+^{242,244}\mathrm{Pu}\rightarrow^{290,292}114^{*}$ reactions. The 3n decay path of $^{292}114^{*}$ could be fitted with spherical fragmentation and hence the exclusive role of β_2 deformations is accessed for the 3n decay path of $^{292}114^{*}$ nucleus. By contrast, the 3n–5n decay paths of $^{290}114^{*}$ and 4n–5n decay paths of the $^{292}114^{*}$ nucleus could only be fitted with β_2 deformations. Deformation effects are therefore important in the study of the decay paths of $^{290}114^{*}$ and $^{292}114^{*}$ nuclei. We have found that the magnitude of the ℓ window for $^{292}114^{*}$ is higher than that for $^{290}114^{*}$. Other important results are as follows: (1) the angular momentum and $E_{\mathrm{c.m.}}$ have no influence upon the fragmentation path in both reactions, independently of the (3n, 4n, or 5n) channel; (2) changes in the N/Z ratio have little effect upon the isotopes of $Z = 114$; (3) ΔV_B is smallest for the highest angular momentum states and higher in magnitude for 3n decay than for 4n decay; (4) the neck-length parameter ΔR is higher for 4n decay than for 3n decay for both the $^{290}114^{*}$ and $^{292}114^{*}$ nuclear systems. Finally, we have predicted the fission and quasi-fission cross sections for the $^{292}114^{*}$ nucleus in the energy range of $E^{*}_{\mathrm{CN}} = 40$–47, which can be checked against measurements when the experimental data become available.

Acknowledgments We are thankful to the Council of Scientific and Industrial research (CSIR), New Delhi, for the support given to this research work. The authors are also thankful to the (anonymous) reviewer for the useful comments and suggestions for better understanding of the manuscript.

References

1. Y.T. Oganessian, J. Phys. G: Nucl. Part. Phys. **34**, R165 (2007)
2. S. Hofmann, Rep. Prog. Phys. **61**, 639–689 (1998)
3. Y.T. Oganessian, et al., Phys. Rev. C **70**, 064609 (2004)
4. P.A. Ellison, et al., Phys. Rev. Lett. **105**, 182701 (2010)
5. Y.T. Oganessian, et al., Phys. Rev. C **69**, 054607 (2004)
6. J.M. Gates, et al., Phys. Rev. C **83**, 054618 (2011)
7. M.G. Itkis, et al., J. Nucl. Radiochem. Sci. **3**, 57 (2002)
8. R.K. Gupta, M. Bansal, Int. Rev. Phys.(I.RE.PHY.) **5**, 74 (2011)
9. M.K. Sharma, S. Kanwar, G. Sawhney, R.K. Gupta, Phys. Rev. C **85**, 064602 (2011)
10. M.K. Sharma, S. Kanwar, G. Sawhney, R.K. Gupta, W. Greiner, J. Phys. G: Nucl. Part. Phys. **38**, 055104 (2011)
11. R.K. Gupta, in *Clusters in Nuclei*, ed. by C. Beck. Lecture Notes in Physics 818, Vol I (Springer, Berlin, 2010), p. 223
12. R.K. Gupta, S.K. Arun, R. Kumar, Niyti, Int. Rev. Phys. (I.RE.PHY.) **2**, 369 (2008)
13. B.B. Singh, M.K. Sharma, R.K. Gupta, Phys. Rev. C **77**, 054613 (2008)
14. Niyti, R.K. Gupta, W. Greiner, J. Phys. G: Nucl. Part. Phys. **37**, 115103 (2010)
15. R.K. Gupta, Niyti, M. Manhas, W. Greiner, J. Phys. G: Nucl. Part. Phys. **36**, 115105 (2009)
16. R.K. Gupta, Niyti, M. Manhas, S. Hofmann, W. Greiner, Int. J. Mod. Phys. E **18**, 601 (2009)
17. K. Sandhu, M.K. Sharma, R.K. Gupta, Phys. Rev. C **85**, 024604 (2012)
18. M. Kaur, R. Kumar, M.K. Sharma, Phys. Rev. C **85**, 014609 (2012)
19. G. Kaur, M.K. Sharma, Nucl. Phys. A **884**, 36 (2012)
20. S.S. Malik, R.K. Gupta, Phys. Rev. C **39**, 1992 (1989)
21. R.K. Gupta, W. Greiner, Int. J. Mod. Phys. E **3**, 335 (1994)
22. G. Sawhney, M.K. Sharma, R.K. Gupta, Phys. Rev. C **83**, 064610 (2011)
23. H. Kröger, W. Scheid, J. Phys. G: Nucl. Part. Phys. **6**, L85 (1980)
24. N.J. Davidson, S.S. Hsiao, J. Markram, H.G. Miller, Y. Tzeng, Nucl. Phys. A **570**, 61c (1980)
25. W. Myers, W.J. Swiatecki, Nucl. Phys. **81**, 1 (1966)
26. P. Möller, J.R. Nix, W.D. Myers, W.J. Swiatecki, At. Data Nucl. Data Tables. **59**, 185 (1995)
27. R.K. Gupta, M. Balasubramaniam, R. Kumar, N. Singh, M. Manhas, W. Greiner, J. Phys. G: Nucl. Part. Phys. **31**, 631 (2005)
28. S. Kumar, R.K. Gupta, Phys. Rev. C **55**, 218 (1997)
29. H.S. Khosla, S.S. Malik, R.K. Gupta, Nucl. Phys. A **513**, 115 (1990)
30. R.K. Gupta, S. Kumar, W. Scheid, Int. J. Mod. Phys. E **6**, 259 (1997)